Antiproton distributions in Au+nucleus collisions

M.J. Bennett,[2] D. Beavis,[1] J.B. Carroll,[3] J. Chiba,[4] A. Chikanian,[2] H.J. Crawford,[5] M. Cronqvist,[5] Y. Dardenne,[5] R. Debbe,[1] T. Doke,[6] J. Engelage,[5] L. Greiner,[5] R.S. Hayano,[7] T.J. Hallman,[3] H.H. Heckman,[8] T. Kashiwagi,[6] J. Kikuchi,[6] B.S. Kumar,[2] C. Kuo,[5] P.J. Lindstrom,[8] J.W. Mitchell,[9] S. Nagamiya,[10] J.L. Nagle,[2] J.K. Pope,[2] P. Stankus,[10] K.H. Tanaka,[4] R.C. Welsh,[11] and W. Zhan[10]

(The E878 Collaboration)

[1]*Brookhaven National Laboratory, Upton, New York*
[2]*Yale University, A.W. Wright Nuclear Structure Laboratory, New Haven, Connecticut*
[3]*University of California at Los Angeles, Los Angeles, California*
[4]*National Laboratory for High Energy Physics (KEK), Tsukuba, Japan*
[5]*University of California Space Sciences Laboratory, Berkeley, California*
[6]*Waseda University, Tokyo, Japan*
[7]*University of Tokyo, Tokyo, Japan*
[8]*Lawrence Berkeley Laboratory, Berkeley, California*
[9]*Universities Space Sciences Research Association/Goddard Space Flight Center, Greenbelt, Maryland*
[10]*Nevis Laboratory, Columbia University, Irvington, New York*
[11]*Johns Hopkins University, Baltimore, Maryland*

(Received 8 April 1997)

Experiment E878 at the BNL-AGS has measured the invariant cross sections of antiprotons produced near $p_t=0$ in interactions of 10.8 GeV/c Au beams with targets of Al, Cu, and Au. The data were measured for a wide range of centralities and rapidities using a focusing beamline spectrometer and a high-rate centrality detector. We compare our data with the predictions of simple models and sophisticated transport models to explore the physics of antiproton production and annihilation. [S0556-2813(97)01209-0]

PACS number(s): 25.75.Dw

I. INTRODUCTION

The study of antiprotons ($\overline{p}$) is a very fertile topic within the field of relativistic heavy ion physics. The observed yield of antiprotons is related to most of the interesting topics in the field, including the formation of nucleon resonances, high baryon density matter, and the formation of a quark-gluon plasma (QGP), as detailed below.

The production of antiprotons at beam energies near (or below) their production energy threshold has been associated with the formation of nucleon and meson resonances [1–5]. Thus, through collective effects, $\overline{p}$ production can be enhanced in $A+A$ collisions as compared to $p+p$ collisions. The formation of resonances allows the system to effectively store energy, which is important for antiproton production near threshold; the high density of the surrounding medium allows the resonances to subsequently undergo multiple interactions even though their lifetime can be as small as a few fm/c.

Beyond the formation of resonances, $\overline{p}$ production could be enhanced in $A+A$ collisions by other, more exotic, means. In particular, the formation of a QGP may significantly increase the yield of antibaryons in $A+A$ collisions. Antimatter production is expected to be enhanced in the QGP, where, due to chiral symmetry restoration (the approximate masslessness of the light quark flavors) antiquarks are expected to be much more abundant than in a hot hadronic gas of the same temperature and baryon density. In a detailed calculation by Heinz, Subramanian, Stöcker, and Greiner [6], $\overline{p}$ yields increase by roughly a factor of 3–5 in a system which has passed through a QGP over those for a hot hadron gas for temperatures between 100 and 200 MeV. Ellis, Heinz, and Kowalski [7], using a Skyrme model, estimate that the antibaryon abundances in the rehadronization phase transition of a QGP the size of a sulfur nucleus and at a temperature of 160 MeV are increased by a factor of 8–12 over an equilibrium hadron gas. Thus, enhanced antimatter production is a promising candidate signature of QGP formation.

However, an overall increase in initial $\overline{p}$ production may not result in an increase in measured yields. After being produced, the $\overline{p}$ must still escape the collision region in order to be detected. In a region of high baryon density this may be difficult because there is a high probability of annihilation of the $\overline{p}$. Thus, in order to clearly recognize the signature of enhanced production, the process of annihilation must also be well understood.

The cross section for annihilation exhibits a very strong dependence on the relative momentum of the baryon-antibaryon pair, and is interpreted as being influenced by the large real portion of the interaction potential [8]. Below 1 GeV/c, the annihilation cross section increases dramatically; at 100 MeV/c, the annihilation cross section has been measured to be $\sim$300 mb [8] which corresponds to an interaction center-to-center separation of $\sim$3 fm, several times as large as the average distance between nucleons at normal nuclear density ($\rho_0 \approx 0.15$ fm^{-3}). Thus, the probability of annihilation for a $\overline{p}$ produced within the interaction volume of a

relativistic heavy ion collision, where the baryon density may be as large as 5–8 ρ_0 [9], is very high indeed.

Simulations have given some indication of how the annihilation process might change in the dense environment of a heavy ion collision. It has been shown that the amount of annihilation in the nuclear medium depends strongly on the formation time of the production process [10,11]. It is also possible that the large particle multiplicities produced in central collisions will affect the amount of $\bar{p}$ annihilation. In the transport models ARC [9] and RQMD version 2.2 [12], probable antiproton-nucleon annihilation partners can be scattered by other particles before actual annihilation occurs, such that the effective annihilation cross section is reduced from that measured in free space. Mean color potentials may also affect the annihilation process, as discussed by Spieles *et al.* [13]. In their description, the baryon-antibaryon interaction potential is broken into real and imaginary parts; at low relative momentum, the real part of the interaction is much larger than the imaginary part. The authors argue that annihilation may be reduced in medium through the cancellation of the real part of the interaction from competing annihilation partners.

We present here antiproton cross sections for Au + A collisions at a beam momentum of 10.8 A GeV/c, as measured by experiment E878 at the Brookhaven National Laboratory Alternating Gradient Synchrotron facility (BNL-AGS). E878 is a high-rate single particle spectrometer designed to study rare processes in high-energy heavy ion collisions, e.g., production of antiprotons [14], and to search for previously undiscovered particles, e.g., strangelets [15]. E878 is a follow-on experiment to E858, which measured antideuteron and antiproton production in Si+A collisions [16]. The data presented in this paper were collected in the September–October 1993 Au beam run.

There are five sequences of experiments which have measured antiproton production from heavy ion induced reactions at the AGS: E858/E878 [16–18], E814/E877 [19,20], E802/E859/E866 [10,21–23], E886 [24], and E864 [26]. Despite some mysteries, the measurements of $\bar{p}$'s from Si beams were perhaps best summed up by Stankus in his thesis: ''[A] simple model based on $p+p$ phenomenology [with minimal absorption] explains almost all of the behavior of $\bar{p}$'s observed'' in Si+A reactions [17]. The inference has been that enhancement in $\bar{p}$ production brought on by the heavy ion environment was counterbalanced by annihilation. Unfortunately, this has made it difficult to determine the details of these processes. In the ARC model, the absorption is screened by a third body interaction and production is enhanced by low-lying resonance production [9]. In the RQMD 1.07 picture, production is substantially enhanced by the formation of high mass resonances; e.g., in minimum bias Au+Au collisions, initial $\bar{p}$ production in RQMD is a factor of ~20 higher than expected from first collisions [28]. This enhancement is then substantially reduced by annihilation, so that for minimum bias Au+Au collisions 90% of the initially produced antiprotons are absorbed. Both of these models match data for Si beams reasonably well [9,10,2,28].

In this work, the production and annihilation processes will be investigated in the context of the target and centrality dependence of $\bar{p}$ yields for a wide range of geometries in the much heavier systems available with Au beams. These results will be compared to predictions based on simple $p+p$ phenomenology, as well as to the more sophisticated model RQMD. E858 observed a broadening of the $\bar{p}$ rapidity distribution for Si+A collisions relative to observations from $p+p$ interactions [16]; a second goal of this work will be to investigate how the widths of the distributions change with target and centrality, and what that might imply about the production mechanism. Finally, it will be possible to extend the work done in Si beams regarding first collision scaling to the truly heavy Au+Cu and Au+Au systems. The linear relationship of $\bar{p}$ yields to interacting beam nucleons reported by E814 [19] was necessarily limited by the number of nucleons available from the Si beam nuclei. Here the range in which this relationship can be studied will be extended to those available in central Au+Au collisions, where the total number of interacting nucleons can reach ~400.

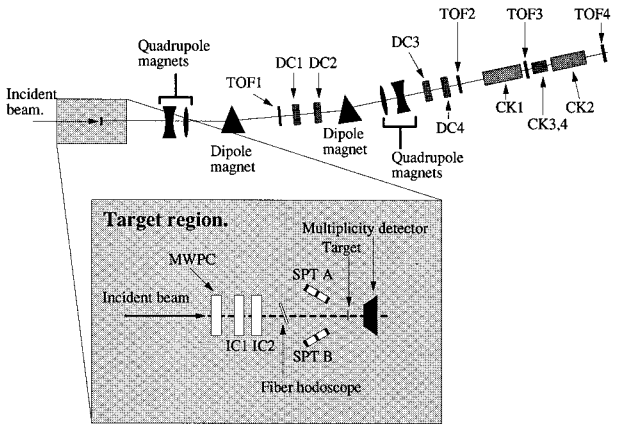

FIG. 1. Schematic of the E878 experimental apparatus, showing sequence of magnetic elements and particle detectors in the beamline. Target area is shown in detail in expanded section. Distances are not to scale.

II. THE APPARATUS

A schematic diagram of the E878 experimental apparatus is shown in Fig. 1. In this diagram the beam enters from the left and impinges on the target. A detailed schematic of the target area detectors is given in the expanded view; the detectors here consist of a multiplicity detector to characterize the collision geometry and several beam monitoring and counting detectors. When a beam particle undergoes an inelastic interaction in the target, any produced secondary particles which fall into the phase space acceptance of the E878 magnetic spectrometer will be transported through its beamline. The beamline and its acceptance are detailed in [18]; roughly, any particle which has a rigidity (ratio of momentum to electric charge, $R \equiv p/Z$) within $\sim \pm 2\%$ of a tuned mean rigidity and a trajectory within ~15–20 mr of the beam direction will be accepted. For the vast majority of beam-target interactions, no particles fall into this phase space region; for roughly one in 10^4 events, a particle will be produced which falls into our acceptance. For these particles, the following characteristics are among those measured: time-of-flight (TOF), trajectory, and whether or not light was generated in several threshold Cerenkov detectors. The time-

of-flight system consists of four separate scintillator based detectors (designated TOF1–TOF4) placed at various locations along the ~60 m length of the spectrometer. The particle's trajectory is measured by four sets of drift chamber detectors, designated DC1–DC4. Finally, there are four threshold Čerenkov detectors, designated CK1–CK4.

As pictured, the E878 spectrometer is capable of measuring production cross sections for secondary particles using Au beam rates up to $\sim 5\times 10^7$ per 1 second AGS spill. If the multiplicity detector and the optical fiber hodoscope are removed from the data stream, the Au beam rate capability increases to (at least) $\sim 2-3\times 10^8$, which was the full intensity of the AGS during the fall 1993 run.

The beam momentum for the Au beam during the 1993 run was measured by the AGS personnel to be 11.086 ± 0.03 GeV/c per nucleon [29]. The E877 Collaboration measured the beam momentum at their target to be 10.78 ± 0.03 GeV/c per nucleon [30]; the difference of these measurements is attributed to beam energy losses between AGS extraction and the E877 target. E878 has no mechanism for measuring the beam energy at our target. For all model comparisons, we have assumed the beam momentum to be 10.8 GeV/c per nucleon. However, it should be noted that the beam energy is not part of the equation to calculate production cross sections (the only energy which is used in calculating cross sections is that of the secondary particles); thus, the uncertainty in the beam momentum does not imply an uncertainty in our measured cross sections, only in the beam energy at which the cross sections have been measured. However, the beam momentum for the fall 1993 Au beam run was different from that for subsequent AGS Au beam runs. Since $\bar{p}$ production near threshold is very sensitive to the beam momentum, it is important to be aware of this quantity when comparing results between experiments.

The heart of the E878 experiment is the beamline, which consists of a double focusing spectrometer. The magnetic elements in the E878 beamline comprise a total of six quadrupole magnets and five dipole magnets. Particles first encounter a pair of quadrupoles which focus the beam in the vertical direction; these are then followed by a pair of quadrupoles which focus the beam in the horizontal direction. Both of the sets of quadrupoles are tuned such that the beam comes to both a vertical and horizontal waist at our first time-of-flight detector (TOF1), located ~35 m from the target (all positions given are measured in z, the distance traveled along the beamline by a particle with the central tuned rigidity). Between the quadrupoles and TOF1, the beam passes through two dipole magnets and undergoes a bend of ~4° to the left (all directions are taken to be from beam view). In conjunction with collimation of the beam by magnet apertures and variable slits, the chromatic dispersion from this bend effectively determines the $\Delta p/p$ acceptance of the beamline. Just before the first waist, the secondary beam is collimated in both the vertical and horizontal directions, via a set of variable jaws. The horizontal portion of this collimator is the defining aperture for $\Delta p/p$. After the first focus, the beam again undergoes horizontal and then vertical focusing, with a common waist for both dimensions to occur at TOF3, located ~62.5 m from the target. The beam also undergoes a second momentum-selecting bend in this downstream section of the beamline, this one being ~8.5° to the left, accomplished via a series of three dipoles.

The primary means of providing particle identification in E878 is via time-of-flight measurements, utilizing two types of time-of-flight detectors: single slat (TOF1 and TOF3) and segmented multislat detectors (TOF2 and TOF4). TOF1 and TOF3 are located at the two waists of the secondary beam where the transverse size of the beam envelope is small. The slats are viewed on each end by a Hamamatsu R2083 photomultiplier tube. TOF2 and TOF4 were located at positions along the beamline where the beam envelope was somewhat larger, so that a multislat design was used. Each of these detectors consist of five slats arranged in two layers, in an alternating fashion, with a horizontal overlap region of ~3 mm between adjacent slats.

The TOF detectors performed very well during data taking. Detection efficiencies for TOF2 and TOF4 were >99 and ~ 95%, respectively. Detection efficiencies for TOF1 and TOF3 could not be directly determined, since these detectors are part of the experiment trigger. However, given the simple design and small size of the detectors, we expect the efficiency to be very close to 100%. The primary measure of TOF for particle identification is the difference between the time of passage at TOF1 and the time of passage at TOF3, with these detectors being separated by ~27.5 m.

There are four Čerenkov detectors utilized in E878, designated CK1–CK4. Of these, CK1 and CK2 are gas based detectors, using freon-12 nominally at 2.77 atm absolute pressure, which are used to distinguish pions from kaons at high rigidity. At the highest rigidities, data were taken using freon-12 at 1 atm absolute in CK1 and with CO_2 at 2.77 atm in CK2, allowing simultaneous pion-kaon and kaon-antiproton separation. CK3 and CK4 utilize silica aerogel with an index of refraction of 1.025 as the Čerenkov radiator and are used to separate pions from electrons and muons at low rigidity. All of the Čerenkov detectors are operated as threshold detectors.

There were four sets of drift chambers, designated DC1–DC4. DC1 and DC2 were used to measure particle trajectories in the upstream half of the beamline, between the two sets of dipoles. This pair of chambers was separated by ~1.5 m. DC3 and DC4 were located downstream of the last magnets, and provide particle trajectory vectors for the downstream portion of the beamline. These chambers were separated by ~5 m. Each chamber consists of a set of seven cathode foils and six anode wire planes, with anode wire spacing of 16.5 mm. The gas used was a mixture of 80% Ar, 20% isobutane (C_4H_{10}).

The drift chambers performed very well during the run of the experiment, with efficiencies found to be ~100%. Spatial resolution of the chambers was better than $\sigma = 100$ μm. The primary use of the chambers during the run was to aid in the tuning of the beamline. For offline analysis, the primary use of the chambers was to provide quality checks for the data, allowing us to reject any events with a track which did not point back to the target or with more than one track in the spectrometer, as well as events with no particle trajectory (which would indicate an accidental trigger). The number of events not passing these cuts was very small, so that their effect on cross sections was negligible; however, the ability to perform these type of cuts was invaluable in the search for new particles [15]. In addition,

the secondary beam profiles as measured by the DC's were used in the calculation of the acceptance of the spectrometer.

The multiplicity detector, described in detail in [31], consists of 28 counters, arranged in two rings oriented at 40° and 60° relative to the beam direction. Each counter consists of a square photomultiplier tube (Hamamatsu R2248SX), topped by a 1/4 in. thick quartz plate, which serves as a Čerenkov radiator, and a 1/4 in. thick lead plate, which corresponds to roughly one radiation length of that material. The lead serves the dual purpose of converting photons into e^+ - e^- pairs and ranging out low-energy δ rays, which are associated with electromagnetic interactions, and thus not related to collision geometry. The array is designed primarily to detect photons from the decays of neutral pions produced in the heavy ion collision, but it is sensitive to any charged particles with $\beta > 0.7$.

Several detectors were used for monitoring both the position and integrated intensity of the beam: two ionization chambers (designated IC1 and IC2); two single particle telescopes (SPT1 and SPT2), a removable thin quartz plate (BC1) for measuring beam particles via Čerenkov radiation, a fiber optic hodoscope with layers segmented in both the horizontal and vertical directions (FIDO), and a multiwire proportional chamber (MWPC). Of these, the latter two are designed primarily to determine the position of the beam, while the IC's and SPT's serve to integrate the number of beam particles into the target area. BC1 is used only for calibration purposes.

All of the beam monitoring detectors are positioned upstream of the target, and within 1 m of the target position. The two ionization chambers, IC1 and IC2, have a circular active area of radius ~ 5 cm, which is considerably larger than the beam spot (~ 2 mm in diameter) and the targets (4 mm vertical by 15 mm horizontal). Thus, these detectors integrate the number of beam particles traversing the region close to the target. Calibration is accomplished by counting beam particles directly at low flux rates using a quartz Čerenkov counter (BC1), and using secondary particle telescopes (SPT1,2) at high flux rates. The IC's were found to become nonlinear at beam rates in excess of 2×10^7 Au ions per 1 sec. spill. This nonlinearity is believed to be caused by recombination of the produced ionization before it can be collected by the chamber.

The single particle telescopes (SPT1 and SPT2) are designed to measure the amount of beam which actually strikes our target. Each SPT consists of three small scintillators of increasing size, ranging from 4 mm square for the element nearest the target to ~ 4 cm square for the element furthest from the target. The scintillators are arranged such that the three are aligned perpendicular to a line which points at the target; the increasing size of the scintillators forms a solid angle such that particles which strike all three elements must have come from the target, with minimal acceptance for sources behind the SPT. Thus, the number of coincidences for an SPT, read out at the end of each spill, is proportional to the amount of beam striking the target. The constant of proportionality will differ according to the target material; these were calibrated at low flux rates using BC1.

The linearity of the SPT's for high beam flux was verified by performing a comparison of SPT counts to IC counts for both Al and Au targets. Since the SPT coincidence rate for Au targets is ~ 4 times that of Al targets, this study confirmed that the nonlinear relation between SPT and IC was a result of recombination in the IC's, not false coincidences in the SPT's. Using the SPT's to calibrate the nonlinearity, the IC's are used as the primary measure of beam flux.

The final beam monitoring detector was a multiwire proportional chamber (MWPC), which was used to determine the spatial profile of the beam. The MWPC was operated with a 75% Ar 25% CO_2 gas mixture and 2 mm spacing between anode wires. The MWPC provided a spill-integrated measurement of the beam profile in the horizontal and vertical directions.

Triggers for E878 are generated by produced particles traversing the spectrometer, allowing E878 to selectively record only particles of interest and thereby enrich the fraction of those events in the data sample. For the analysis in this paper, two types of triggers are utilized: LOOSE, which consists of a coincidence between TOF1 and TOF3, is created by any particle in the spectrometer and thus contains primarily pions for negative rigidity running; and PIBAR, which is a subset of LOOSE with the addition of a veto from the Čerenkov detectors, so that it selects slow particles, i.e., kaons and antiprotons. E878 also utilized other triggers which were designed to select particles more massive (and thus slower) than antiprotons. These triggers were used primarily for the search for new particles [15]. By downscaling triggers from copiously produced particles, i.e., pions, we are able to enrich the rare particle fraction of our data sample. LOOSE prescale values ranged between 10–100 for the negative running.

Since E878 triggers on particles in the spectrometer (with no precondition on the nucleus-nucleus interaction), the cross sections which we measure are truly minimum bias spectra. However, using the multiplicity detector described above, it is possible for us to determine the centrality of the collision which produced the detected particle, and to characterize the detected particles in bins of interaction centrality. The calibration and performance of the multiplicity detector is described in detail in [31]. It was possible for us to define four multipicity bins for Au+Au interactions: peripheral (the 30% lowest multiplicity interactions, or 100–70 % of the geometric cross section), midperipheral (70–30 % of geometric cross section), midcentral (30–10 % of geometric cross section), and central (the 10% highest multiplicity interactions). We also defined central bins for Au+Cu (11% highest multiplicity) and Au+Al (12% highest multiplicity) interactions.

In order to investigate the target and centrality dependence of antiproton production, three different target materials of varying nuclear size (Al, Cu, and Au) were utilized, and eight rigidities were sampled for each target type: -8.0, -6.0, -4.4, -3.87, -3.2, -2.2, -1.8, and -1.5 GeV/c. Of these, the first six cover the antiproton kinematic range from nucleon-nucleon center-of-mass rapidity ($y_{nn} = 1.57$) to (almost) beam rapidity. The lowest two settings, -1.8 and -1.5, pushed the limits of the beamline (in terms of multiple scattering). However, these settings were thought to be very important, since they were below y_{nn}, which would allow an investigation of rapidity shifts in the asymmetric light target systems, as well as provide a redundant check on other mea-

surements (via reflection about y_{nn}) in the symmetric Au+Au system.

After quality cuts were applied to the data, good target and centrality information, covering a large kinematic range, was obtained for $\sim 10\,000$ antiprotons. This represents the highest statistics investigation of antiproton production performed in relativistic heavy ion collisions at the AGS to date.

III. DATA ANALYSIS

We will outline the data analysis procedure; the entire analysis procedure is described in detail in [18]. Our operational definition for the invariant cross section is (in units of mb $\mathrm{GeV}^{-2}\ c^3$)

$$E\frac{d^3\sigma}{dp^3}=[N_{\mathrm{detected}}-(R_{\mathrm{to}}N_{\mathrm{beam}}\varepsilon_{\mathrm{live}})]\times\frac{\eta_{\mathrm{reint}}}{N_{\mathrm{beam}}\times N_t\times a\times\varepsilon_{\mathrm{live}}\times\varepsilon_{\mathrm{PID}}\times\varepsilon_{\mathrm{thick}}\times(p^3/E)}, \quad (1)$$

where N_{detected} is the number of detected particles with momentum $\vec{p}\pm\Delta\vec{p}$, N_{beam} is the number of incident beam particles, and N_t is the number of target nuclei per unit area. The acceptance of the apparatus a is given in terms of the solid angle and a momentum spread $\Delta p/p$, and has been determined by comparing measured particle trajectories to TURTLE [32] and TRANSPORT [33] simulations of the beamline. Other corrections and efficiencies are as follows: particle identification efficiency $\varepsilon_{\mathrm{PID}}$, which includes contributions for the efficiency of the detector to trigger on and record a particle in the spectrometer, as well as the efficiency of the analysis cuts employed to identify the particle, livetime correction $\varepsilon_{\mathrm{live}}$, which quantifies the fraction of time the data acquisition system is live and able to respond to triggers, target out correction R_{to}, which corrects for the rate at which particles are produced from nontarget sources, reinteraction correction η_{reint}, which corrects for losses of particles via inelastic interactions in material in the beamline, and the thick target correction $\varepsilon_{\mathrm{thick}}$, which accounts for loss of beam flux as it traverses the target.

By its design, E878 directly measures production cross sections for particles. For convenience in comparing to models and other experiments, these cross sections can be converted to invariant multiplicity, using

$$\frac{d^3N}{dp^3}=\frac{1}{\sigma_{\mathrm{in}}}\frac{d^3\sigma}{dp^3}, \quad (2)$$

where σ_{in} is the inelastic cross section for interaction between the beam and target nuclei. Interaction cross sections between two nuclei for minimum bias events are estimated by the parametrization given by Hoang, Cork, and Crawford [34], which yields interaction cross sections of 6850 mb for Au+Au, 4700 mb for Au+Cu, and 3750 mb for Au+Al. More exclusive classes of events (e.g., 10% central events) are assigned the appropriate fraction of these total interaction cross sections.

Before attempting to identify a particle, quality cuts based on trajectory information are applied to events. The requirements for a good event are: a single track in the spectrometer, a track which projects back to the target (this consists of a cut in the angle of the track with respect to the beam at TOF1) and a track whose projection lies within the active region of the TOF3 scintillator. The fraction of events cut out by these requirements is small, and these cuts are taken to create no inefficiency in the counting of real particles.

Velocity for a particle is determined by comparing its measured TOF to the TOF for a particle traveling with a velocity $v=c$, where this latter quantity can be determined simply by knowing the path length traversed by the particle. (Due to the 62.5 m extent of the beamline and the small transverse size of the beam envelope, the differences in path lengths of particles are on the order of 10^{-5} of the total path length, and have a negligible effect on the measured TOF.) Thus, the relativistic velocity measured for a given event is

$$\beta=\frac{v}{c}=\frac{\mathrm{TOF}(\beta=1)}{\mathrm{TOF(measured)}}. \quad (3)$$

Combining the momentum (p), known from the beamline optics, with the measured velocity, it is possible to determine the mass of the particle. In practice, particle identification (PID) is done simply in TOF space.

For all rigidities considered here, π^-'s can be unambiguously identified with high efficiency using Čerenkov information; thus the primary challenge is to separate antiprotons from K^-'s. The path length between TOF1 and TOF3 is $\sim$27.5 m, which is sufficiently long that antiprotons are well separated ($>4\sigma$) in time-of-flight over that distance (T13) from K^- for all rigidities below 6.0 GeV/c. There is some background in the T13 spectrum which is not associated with real particle peaks, and which can be ascribed to various sources: inelastic interactions of particles in the material in the beamline, false triggers caused by a random firing of a TOF1 tube followed by a real particle in the spectrometer, pions from K^- decays as they proceed down the beamline, etc. This background can be eliminated by requiring the time between TOF2 and TOF4 to be consistent with that between TOF1 and TOF3. The flight path between TOF2 and TOF4 is $\sim$12.5 m, which is roughly 0.45 times the TOF3-TOF1 distance, so that all events have been required to satisfy the condition $|[T24-(T13\times 0.45)]|<2$ ns. A sample plot of T24 vs T13 for a rigidity of -2.2 GeV/c is shown in Fig. 2. The cleanliness of the T13 spectrum surviving this cut can be seen in Fig. 3 which shows sample PID plots for a rigidity of -3.2 GeV/c. In this case, π^-'s (shown in the upper plot) have been identified by requiring both of the gas Cerenkov detectors to fire (as determined by the ADC's from these detectors). The lower plot shows TOF spectra for events without a gas Čerenkov signal; both K^-'s and antiprotons fall into this category for this rigidity. Valid ADC signals are required from all of the PMT's in the slats which were struck.

As stated earlier, the $\overline{p}$ T13 peak is well separated from that of the K^- for all rigidities less than 6 GeV/c. For all of these rigidities, the identification of antiprotons was performed by fitting the T13 peak to a Gaussian; a cut of $\pm 3\sigma$ from the mean of this fit was then used to identify antiproton events.

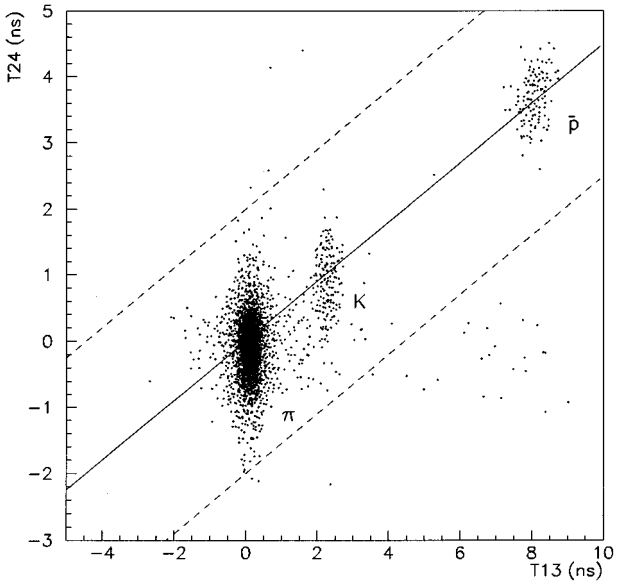

FIG. 2. T24 vs T13 for a rigidity of -2.2 GeV/c. Solid line indicates agreement between T13 and T24 based on relative path lengths, dashed lines indicate the region satisfying the ± 2 ns T13-T24 agreement cut.

Matters become somewhat more complicated for the two highest rigidity settings. At 6.0 GeV/c, the T13 peaks for K^-'s and $\overline{p}$'s are overlapped to some degree, as can be seen in the sample PID plot shown in Fig. 4. Unfortunately, K^-'s are still below the threshold for firing the gas Cerenkov detectors while both kaons and antiprotons are above threshold for the aerogel Cerenkov detectors so that the Cerenkov detectors are not useful for $K^- - \overline{p}$ separation. Thus, antiprotons have been counted using a double Gaussian fit to the T13 spectrum. The mean values for the two Gaussians were not constrained; however, the differences between means resulting from the fits were consistent with T13 expected for K^-'s and $\overline{p}$'s for this rigidity.

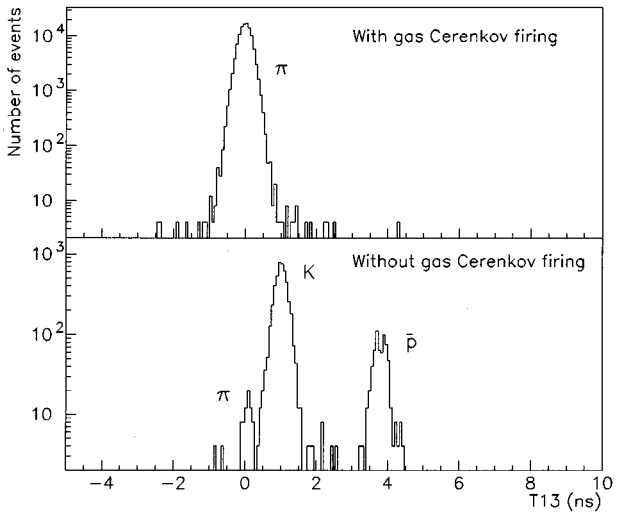

FIG. 3. Sample T13 distributions for a rigidity of -3.2 GeV/c, with T13-T24 agreement cut applied. Upper plot is with gas Cerenkov detectors firing; lower plot is without gas Cerenkov firing.

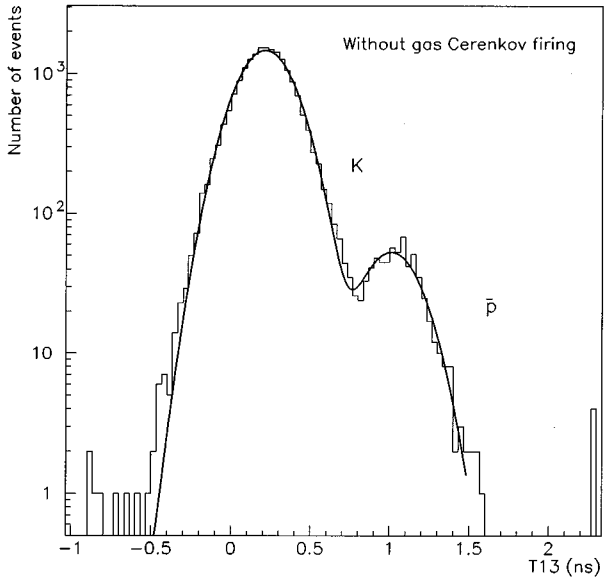

FIG. 4. Double Gaussian fit to $K^- - \overline{p}$ peak for -6.0 GeV/c.

For the highest rigidity (8.0 GeV/c), PID is accomplished simply by Cerenkov information. For this rigidity, the downstream gas Cerenkov detector (CK2) was operated in the ''normal'' configuration of 2.77 atm Freon-12, while the upstream gas Cerenkov detector (CK1) was operated at 1.0 atm Freon-12. In this configuration, both kaons and pions should fire CK2, while only pions should fire CK1; $\overline{p}$'s should fire neither detector. The primary concern in counting $\overline{p}$'s in this manner is contamination from K^- resulting from inefficiency of CK2. To estimate this background, the CK2 ADC peak is fit to a Gaussian distribution for events which do not fire CK1; these are nominally K^- events. This fit is performed over the truncated mean ADC distribution (i.e., only those ADC values which correspond to the lower 60% of the events in the entire distribution) so that the high-side tail of the Poisson distribution is discarded and the remaining events should be roughly Gaussian. Based on this procedure, a cut of 20 (and below) on the CK2 ADC has been placed, which should reduce the K^- contamination to $\sim 5\%$ of the $\overline{p}$ peak.

In E878, there is a non-negligible amount of material in the path of the beam upstream of the target which includes windows and gas for both ion chambers and the multiwire proportional chamber, optical fibers in the fiber optic hodoscope, vacuum windows in the upstream magnets, as well as a substantial length of air between the last magnet and the target. In total, this material constitutes roughly a 4–5 % interaction length target for the Au beam. In order to quantify the amount of this nontarget related background, a slot on the target wheel was left empty and, for each rigidity, data were taken with this empty target in place which were used to calculate a nontarget related production rate for antiprotons, R_{to}. The number of observed antiprotons for target out was converted to a target out rate by dividing by the total amount of beam flux, corrected by the live time. Then, for each set of data with real targets, the number of observed antiprotons which come from nontarget interactions can be calculated by multiplying this target out rate by the flux and the live time for that set of data. In general, the target out

TABLE I. Minimum bias invariant cross sections for antiprotons. Errors are statistical only.

Rigidity (GeV/c)	Invariant cross section Minimum bias (mb/GeV$^{-2}c^3$)		
	Au+Al	Au+Cu	Au+Au
−1.5	8.99±1.41	13.51±1.36	17.63±2.07
−1.8	N/A	8.64±1.15	13.43±1.50
−2.2	6.02±0.41	10.43±0.51	17.80±1.00
−3.2	5.33±0.28	7.42±0.37	11.58±0.67
−3.87	3.39±0.18	5.92±0.28	10.14±0.38
−4.4	3.28±0.22	5.50±0.33	7.26±0.31
−6.0	0.68±0.05	1.76±0.09	2.79±0.12
−8.0	0.18±0.02	0.49±0.04	1.41±0.09

TABLE II. Minimum bias invariant multiplicity for antiprotons. Errors are statistical only.

Rigidity (GeV/c)	Invariant multiplicity Ed^3N/dp^3 (GeV$^{-2}c^3$)		
	Au+Al	Au+Cu	Au+Au
−1.5	$2.39\pm0.36\times10^{-3}$	$2.88\pm0.29\times10^{-3}$	$2.56\pm0.29\times10^{-3}$
−1.8	N/A	$1.84\pm0.24\times10^{-3}$	$1.96\pm0.22\times10^{-3}$
−2.2	$1.61\pm0.12\times10^{-3}$	$2.22\pm0.11\times10^{-3}$	$2.60\pm0.14\times10^{-3}$
−3.2	$1.43\pm0.06\times10^{-3}$	$1.58\pm0.08\times10^{-3}$	$1.69\pm0.09\times10^{-3}$
−3.87	$9.05\pm0.47\times10^{-4}$	$1.27\pm0.06\times10^{-3}$	$1.48\pm0.05\times10^{-3}$
−4.4	$8.75\pm0.57\times10^{-4}$	$1.17\pm0.07\times10^{-3}$	$1.06\pm0.04\times10^{-3}$
−6.0	$1.81\pm0.13\times10^{-4}$	$3.75\pm0.19\times10^{-4}$	$4.07\pm0.17\times10^{-4}$
−8.0	$4.82\pm0.69\times10^{-5}$	$1.05\pm0.08\times10^{-4}$	$2.06\pm0.13\times10^{-4}$

correction reduces the number of observed antiprotons by 10–20 %. Since the estimated material upstream of the target constitutes ~4% of a Au interaction length, and the targets interact with ~22–27 % of the Au beam, this fraction is consistent with our expectations.

As a cross-check of the time-of-flight information and the tuned rigidity of the beamline, it is possible to calculate the central momentum of the secondary beam based on T13 differences for pions and antiprotons. For all rigidities, the calculated momentum agrees with the nominal momentum to within ±2.5%. For calculation of cross sections, the calculated momentum has been used. Final results for minimum bias invariant cross sections for various targets are given in Table I. Invariant multiplicities are given in Table II for minimum bias and in Table III for the defined centrality cuts. In these tables, only statistical errors are given. In addition, systematic uncertainties of 10% are expected for comparison of cross sections between rigidities; a total systematic uncertainty of 20% is expected in the overall normalization. The dominant factors in the systematic uncertainties are the acceptance and beam flux normalization.

IV. RESULTS AND DISCUSSION

The goals of this analysis are threefold: (1) investigate the shape of the rapidity distributions, how these change with varying targets and centrality, and to compare the distributions to those expected from simple p-p phenomenology; (2) investigate the dependence of $\overline{p}$ yields on the number of participating nucleons in the context of a first collision model; (3) compare the E878 results to predictions from the model RQMD [35].

Shown in Fig. 5 are the invariant multiplicities for $\overline{p}$'s, as a function of rapidity, for minimum bias and 10% central Au+Al, Cu, and Au events. Although not shown here, the E878 Au+Au minimum bias cross sections are consistent within systematic errors with the yields measured in Au+Pt collisions by E886 [24]. All of the distributions seem roughly Gaussian in shape, a trend which is consistent with the observations of E858 for $\overline{p}$'s from minimum bias Si+A collisions [17]. There is a distinct increase in production at high rapidities for the heavier targets, while production at midrapidity is roughly equal for all targets. This trend leads to a broadening of the rapidity distributions for the heavier systems; this broadening is not consistent with the observations of E858, which saw no target dependence in the RMS widths of $\overline{p}$ rapidity distributions for minimum bias Si+Al, Cu, and Au [17].

Also shown in Fig. 5, a similar trend can be seen in the centrality dependence on $\overline{p}$ yields in Au+Au collisions, using four centrality bins. The overall yield in the most peripheral bin is well below that of the more central events. As the centrality, and thus the size of the interaction region, increases, there is a broadening of the rapidity distribution.

TABLE III. Antiproton invariant multiplicity ($\times10^5$) for various bins in event centrality. Errors are statistical only.

Rigidity GeV/c	$10^5\times$ Invariant multiplicity (GeV$^{-2}c^3$)					
	Au+Al	Au+Cu	Au+Au			
	Central 12%	Central 11%	Peripheral 100–70 %	Midperipheral 70–30 %	Midcentral 30–10 %	Central 10%
−1.5	309±115	374±82	254±70	227±35	331±59	255±71
−1.8	N/A	268±75	67.7±44.0	240±31	267±46	238±59
−2.2	185±32	323±34	138±27	302±22	344±33	283±41
−3.2	148±21	202±23	49.7±16.9	216±15	219±22	231±30
−3.87	77.8±13.0	161±19	56.4±9.0	173±8	213±13	194±18
−4.4	95.8±17.3	136±22	51.6±8.1	113±7	146±11	162±16
−6.0	23.8±4.08	51.5±6.8	10.2±2.6	49.6±2.84	62.0±4.3	69.9±6.7
−8.0	5.45±2.05	21.6±3.4	5.53±1.9	19.6±1.9	35.7±3.8	40.8± 5.7

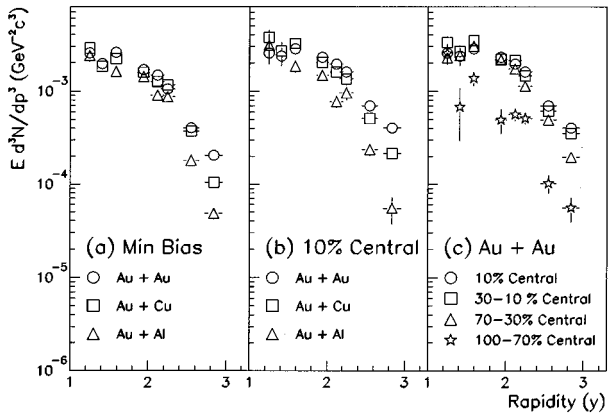

FIG. 5. Target and centrality dependence of the E878 $\overline{p}$ rapidity distributions. Plot (a) shows the target dependence of minimum bias Au+*A* collisions; plot (b) shows the target dependence of 10% central Au+*A* events; plot (c) shows the centrality dependence for the four defined centrality bins in Au+Au events.

This broadening is similar to that seen in target comparisons, in the sense that it arises from an increase in $\overline{p}$ yields at high rapidity, with production near midrapidity remaining roughly constant for the three most central bins. To quantify the amount of broadening, $\overline{p}$ rapidity distributions for each of the four centrality bins from Au+Au collisions are shown in Fig. 6. Each distribution is reasonably well described by a Gaussian in rapidity, with rms widths which increase from 0.48 ± 0.04 units of rapidity for the most peripheral events to 0.62 ± 0.03 for the most central events.

Several different physical processes can lead to a broadening of the rapidity distributions. Production at high rapidity can be enhanced by increasing the available energy in the binary collision leading to the formation of the $\overline{p}$, beyond that available in simple collisions of a beam rapidity nucleon

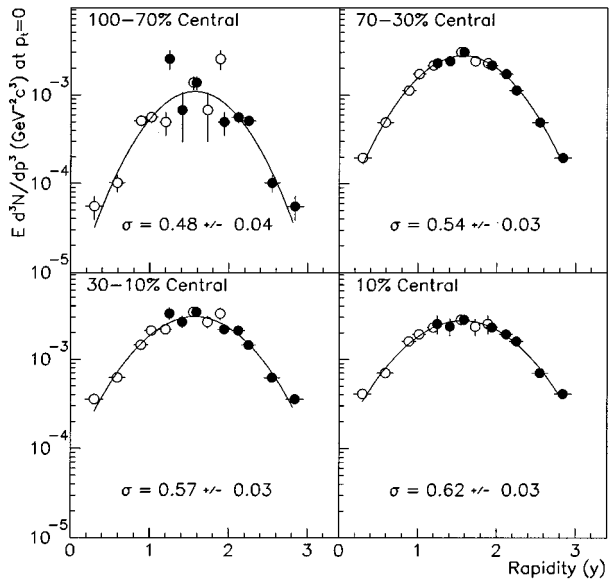

FIG. 6. Centrality dependence of the widths of $\overline{p}$ rapidity distributions for Au+Au events, for defined centrality bins. Solid symbols are measured data; open symbols are reflections of measured data about y_{nn}.

with a target rapidity nucleon. This increased energy can be a result of the formation of nucleon resonances, as well as from Fermi momentum of the nucleons within their respective nuclei. Also, an effective broadening can occur by a depletion of $\overline{p}$'s near midrapidity. Since nearly complete stopping of the nucleons occurs in central Au+Au collisions [36] and the $\overline{p}$-p annihilation cross section increases sharply for low relative momentum [37], antiprotons near midrapidity should have the highest likelihood of being annihilated. Finally, hydrodynamic expansion of the system can lead to a broadening of the rapidity distributions. This phenomena has been investigated for central Si+Al collisions elsewhere [38] for various particle species. All of these processes (and perhaps others we have overlooked) are likely to have contributed in some fashion to the broadening observed by E878. Another open question is how the feeding of $\overline{p}$ states from $\overline{\Lambda}$ decays affects the observed $\overline{p}$ distribution. Simulations of the E878 acceptance indicate that for $\overline{\Lambda}$'s near midrapidity, the acceptance for $\overline{p}$ decay daughters is $\sim 15\%$ of the nominal acceptance; however, for $\overline{\Lambda}$'s near beam rapidity, the relative decay daughter $\overline{p}$ acceptance increases to $\sim 40\%$ of the nominal E878 acceptance.[1] Thus, if the $\overline{\Lambda}$ rapidity distribution is similar to that of the primodial $\overline{p}$'s, then the level of $\overline{\Lambda}$ ''contamination'' of the $\overline{p}$ distribution would increase for increasing rapidity. This would also lead to a broadening of the $\overline{p}$ distribution as observed by E878. However, since the initial level of $\overline{\Lambda}$ production is still unknown, it is not possible to determine the magnitude of this effect.

Generally speaking, the physics of $\overline{\Lambda}$ production is one of the more interesting puzzles in relativistic heavy ion physics today. Direct measurements of $\overline{\Lambda}$ yields from Si+*A* interactions at the AGS indicate a $\overline{\Lambda}$ to $\overline{p}$ ratio well above 1 [23,25], considerably larger than would have naively been expected. How this ratio changes in the much larger Au+*A* systems is an intriguing question. Given that E878 is a single particle spectrometer, this is a topic which we cannot address directly; however, because of our low acceptance for $\overline{p}$'s from $\overline{\Lambda}$ decays, the E878 $\overline{p}$ spectra can serve as a relatively clean ''control'' for comparison to experiments whose $\overline{p}$ spectra include contributions from $\overline{\Lambda}$ decay. Comparisons between the E878 data and antiproton spectra from E864, which accepts nearly all $\overline{p}$'s from $\overline{\Lambda}$ decays, suggest that the $\overline{\Lambda}/\overline{p}$ ratio in central Au+Au(Pb) interactions is also well above 1 [26]. Direct measurements of the $\overline{\Lambda}$ yields in Au+*A* collisions should be forthcoming soon [27].

As a point of comparison, the width of the zero degree $\overline{p}$ rapidity distribution can be calculated based on phase space considerations only, in the simple picture of $\overline{p}$ production resulting only from the collision of a single beam rapid-

[1]These $\overline{\Lambda}$ acceptance figures supercede earlier calculations which have appeared elsewhere [15] and which used idealized assumptions. With renewed interest in the $\overline{\Lambda}$ contribution to our data (as detailed in the text), a more rigorous acceptance calculation was undertaken, yielding these improved results.

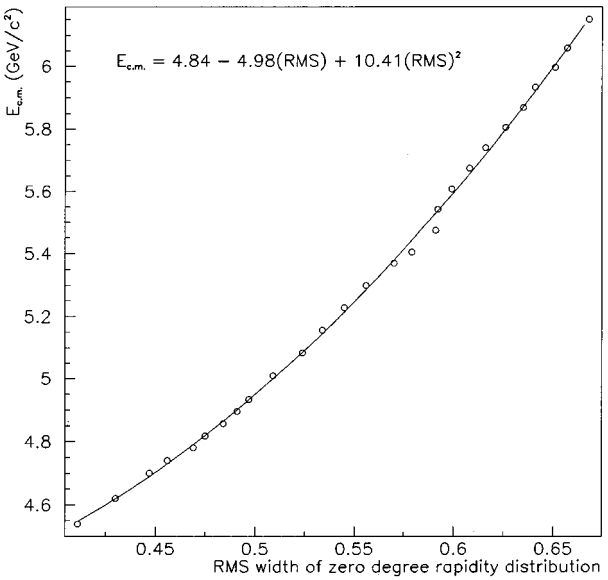

FIG. 7. Parametrization of the total N-N center-of-mass energy $E_{\text{c.m.}}$, as a function of the rms width of the zero degree $\overline{p}$ rapidity distribution. The parametrization is based on the results of a Monte Carlo phase space calculation, with the assumption that $\overline{p}$ production occurs via the reaction $N+N \rightarrow N+N+p+\overline{p}$.

ity nucleon with a single target rapidity nucleon. Assuming that complete stopping occurs in a given nucleon-nucleon collision, then all of the kinetic energy available in the CM frame (after the formation of particles) can be shared nonpreferentially by all products of the collision.[2] Monte Carlo phase space distributions of antiprotons produced via the simplest $\overline{p}$ production process, $N+N \rightarrow N+N+p+\overline{p}$, have been generated using GENBOD, a subroutine available in the CERN libraries [40]. The E878 acceptance is roughly simulated by placing a $p_t < 100$ MeV cut on all particles. A plot of total energy in the center-of-mass frame $E_{\text{c.m.}}$, versus the rms width of the zero degree antiproton rapidity distribution as determined in this calculation is shown in Fig. 7.

The width of the most peripheral measured distribution (0.48 ± 0.04) is consistent with this calculation, which predicts a width of 0.45 for the nominal beam momentum of 10.8 GeV/c. This finding is consistent with the expectation that, for these peripheral events, both collective effects and annihilation are minimal, and $\overline{p}$ production can be well described by a simple N-N picture. However, in order to explain the width of the E878 central distribution, a center-of-mass energy of ~ 5.8 GeV is required; for comparison, $E_{\text{c.m.}} = 4.7$ GeV for the nominal 10.8 GeV/c beam momentum. If nucleon resonances are formed, the kinetic energy available to the produced $\overline{p}$ can increase, thus broadening the rapidity distribution. For example, in the case where beam and target nucleons are each excited to $\Delta(1232)$ resonances, but still have their same momentum in the c.m. frame, the center-of-mass energy would increase to 5.46 GeV. This extra energy alone is not sufficient to explain the width of the central distribution. Broadening due to Fermi momentum of the nucleons within the colliding nuclei is calculable, and is also not sufficient to explain the observed width.

Admittedly, these calculations are simplistic and make some nonphysical assumptions. However, the aim here is to show that, while increasing the available center-of-mass energy can broaden the $\overline{p}$ distribution, it is probably not sufficient to explain the amount of broadening seen by E878, and other processes must also be involved. More importantly, in the absence of annihilation, increasing the center-of-mass energy would increase the overall yield of $\overline{p}$'s for all rapidities, in addition to broadening the distribution. In order to investigate how the total yield of $\overline{p}$'s varies with target and centrality, first collision scaling will be utilized, similar to the approach used to successfully reproduce measured $\overline{p}$ yields in Si+nucleus collisions [10,17,24,11].

A first collision model is attractive in the sense that it represents a simple approach to the problem of modeling $\overline{p}$ production. (A first collision refers to the interaction of a beam nucleon with a target nucleon, neither of which have undergone any previous interactions.) The primary argument in favor of a first collision model is that, in the absence of collective effects, initial $\overline{p}$ production should be proportional to the number of first collisions; this assumed proportionality is predicated on the fact that the kinetic energy in a first collision is only just above threshold, and any further collisions will reduce the available energy even further. However, this is not to say that a first collision model accurately describes the physics of antiproton production/annihilation in a heavy ion collision; the linear dependence of $\overline{p}$ yields on the number of participating beam nucleons, observed by the E814 Collaboration [19], effectively rules out this simplistic picture, as the authors of that paper point out. This is, of course, no surprise— production must be enhanced by collective effects, as clearly shown by subthreshold $\overline{p}$ production observed at the BEVALAC [1], and annihilation (at some level) must occur; a first collision model considers neither of these important processes. Rather, the proper use of first collision scaling is as a benchmark indicating what level of $\overline{p}$ production might be expected from the superposition of the appropriate number of independent nucleon-nucleon collisions, and whether $\overline{p}$ yields are suppressed or enhanced relative to this simple picture.

The number of nucleon-nucleon first collisions, as well as the total number of participant nucleons, corresponding to the collision geometry of the defined centrality bins was determined via Monte Carlo [18,31]. The total yield of $\overline{p}$'s is determined by integrating the measured rapidity distributions, using a rectangular approximation (rather than a functional fit). The range of the integration has been restricted to forward rapidities, i.e., greater than midrapidity.

Shown in Fig. 8 are the total yields, plotted versus the mean number of first collisions. As the size of the interacting

[2]This assumption is not completely valid, even though complete stopping of protons has been observed for Au+Au collisions. This complete stopping is understood to result from a multistep process, whereby each nucleon undergoes a number of collisions, with each individual collision having less than complete stopping [39]. Thus, this approximation represents an upper limit on the kinetic energy available to antiprotons in simple N-N collisions.

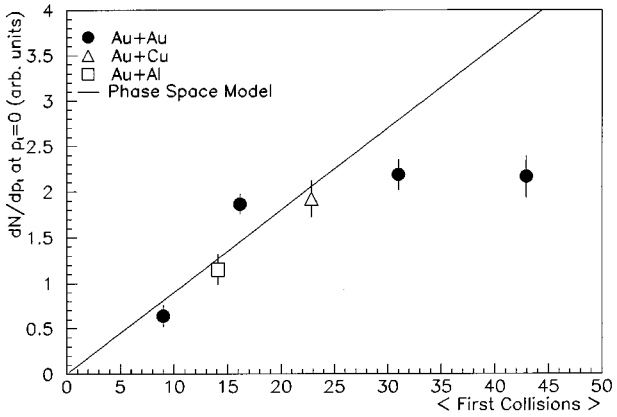

FIG. 8. Total integrated $\bar{p}$ yield into the E878 acceptance for Au+A collisions of various centrality, plotted as a function of the mean number of first collisions. The solid line is the prediction of our phase space/first collisions model (see text for details).

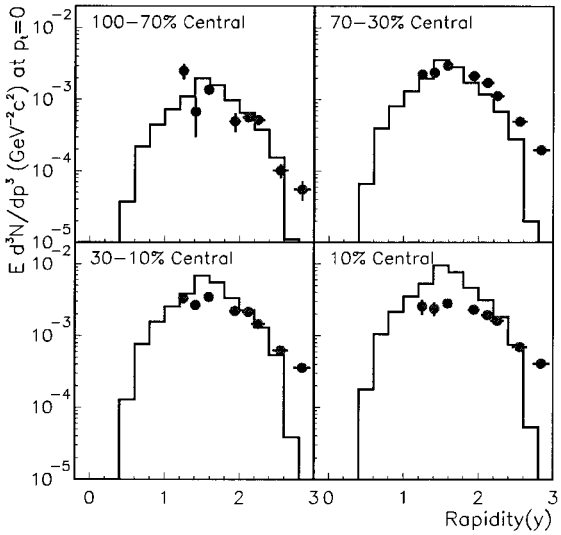

FIG. 9. Comparisons of the results of an N-N first collision model to E878 $\bar{p}$ measurements, for each of the defined centrality bins in Au+Au collsions. Model predictions are shown as histograms and E878 data are shown as symbols.

system increases, the total yield at zero degrees deviates substantially from a linear dependence on the number of first collisions. For smaller Si+A systems, a linear dependence of $\bar{p}$ yields on the number of interacting beam nucleons was observed by the E814 Collaboration [19]; this dependence was taken to infer that the enhancement of production in the heavy ion environment was approximately equal to the amount of annihilation, such that the two processes negated each other. However, for the much larger systems available with Au beams, this linear dependence no longer holds.

In order to set the scale for the $\bar{p}$ yield per nucleon-nucleon interaction, 200 000 RQMD $p+p$ events at a beam momentum of 11 GeV/c were utilized. Of these, ~190 000 had impact parameters which lie inside the 30 mb inelastic cross section used to calculate the number of first collisions. In this subset of events, there were 364 $\bar{p}$'s produced in the E878 acceptance. Correcting for the antimatter enhancement used in this version of RQMD (a factor of 10), the predicted mean $\bar{p}$ yield per p-p interaction is $\langle N_{\bar{p}} \rangle = 1.92 \times 10^{-4}$. This factor has been used to generate the straight line in Fig. 8, which indicates the expected total zero degree yield if all $\bar{p}$ production occurred via simple N-N collisions. For the largest systems, the observed yields are substantially suppressed from this naive picture.

This result could be interpreted as an imbalance in enhanced production and annihilation; however, as will be detailed below, it is possible that some fraction of this observed suppression could be attributed to the boosting of antiprotons away from $p_t = 0$ as a result of hydrodynamic expansion of the system. Nevertheless, it is significant that the observed nonlinearity of total $\bar{p}$ yields occurs in the form of a suppression for heavier systems. Theoretical calculations indicate that antimatter yields from a QGP should be significantly increased (factor of ~3–10 depending on the model) as compared to that from a hadron gas with the same thermodynamic conditions [6,7]. Even allowing for possible effects of hydrodynamic expansion, the E878 data do not appear to be consistent with such a large enhancement in production.

Combining the RQMD scale factor with the phase space distributions from GENBOD (as described above), and the number of first collisions as determined by Monte Carlo, it is possible to predict the expected E878 $\bar{p}$ rapidity distributions in this simplistic phase space/first collisions model. The predicted invariant multiplicity is given by

$$\frac{d^3N}{dp^3}(A+A) = \langle N_{\bar{p}} \rangle \times \langle N_{\text{first}} \rangle \times \frac{1}{\eta} \frac{d^3N(p+p \text{ from phase})}{dp^3},$$

where

$$\eta \equiv \int \frac{d^3N(p+p \text{ from phase})}{dp^3} d^3p. \tag{4}$$

Shown in Fig. 9 are the predictions of the phase space/first collisions model compared to E878 results for Au+Au collisions of varying centrality. The simple model matches the data quite well for the two most peripheral bins, corresponding to the smallest systems, consistent with the first collision scaling of measured $\bar{p}$ yields seen in Si+A collisions [10,17,24]. However, for the two most central bins, the phase space/first collisions model does a poor job of reproducing the data. Some of this discrepancy is undoubtedly the result of $\bar{p}$ annihilation near midrapidity; however, this process is not easy to include in this simple model, and is best addressed by the more sophisticated model RQMD. However, it is also probable that some of the discrepancy can be attributed to hydrodynamic expansion of the interaction region.

Before considering expansion of the system, a final point on these comparisons is in order. For all of the various centrality bins, including the most peripheral, the phase space/first collisions model substantially underpredicts the yield at the highest rapidity point, and for good reason: given the available energy in the c.m. frame, any rapidities above ~1 rapidity unit in the c.m. frame should be kinematically forbidden. In the lab frame, these limits correspond to rapidities

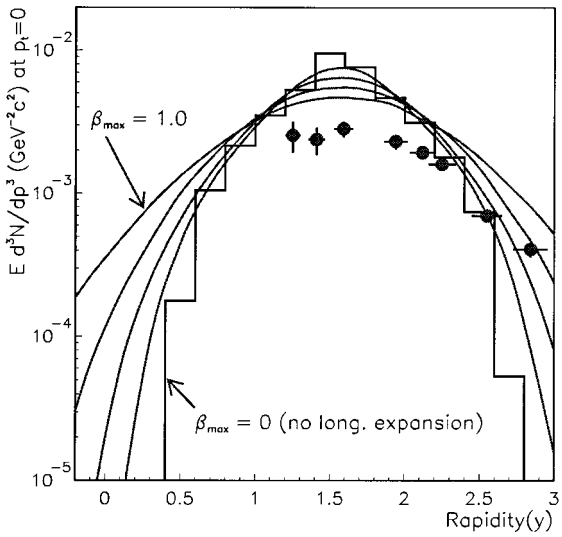

FIG. 10. Comparison of the results of a longitudinal expansion model to E878 $\bar{p}$ data from central Au+Au events. The histogram corresponds to the prediction for $\beta_l^{\max}=0$ (no expansion); smooth curves are predictions for $\beta_l^{\max}=0.4,0.6,0.8,1.0$, with increasing β leading to increased width. E878 data are shown as symbols.

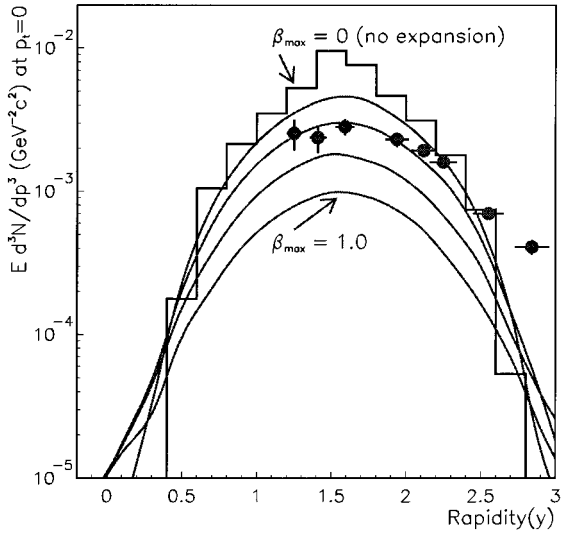

FIG. 11. Comparison of the results of a radial expansion model to E878 $\bar{p}$ data from central Au+Au events. The histogram corresponds to the prediction for $\beta_{\rm rad}^{\max}=0$ (no expansion); smooth curves are predictions for $\beta_{\rm rad}^{\max}=0.4,\ 0.6,\ 0.8,\ 1.0$, with increasing β leading to increased width and decreased overall zero degree yield. E878 data are shown as symbols.

of ~ 0.4 and ~ 2.7; the highest point for E878 is at a lab rapidity of 2.84. However, even for the most peripheral bin, E878 observes $\bar{p}$'s beyond this kinematic limit. Since significant expansion of the system for these peripheral collisions is not expected, $\bar{p}$ production at this high rapidity must be attributed to increased energy in the c.m. frame, brought about by Fermi momentum of the original nucleons, or by resonance formation.

To investigate how system expansion can affect the zero degree $\bar{p}$ spectrum from the 10% most central Au+Au events, consider first a physically unlikely but illustrative example, where expansion is considered to occur in the longitudinal dimension only. Starting with the phase space calculation described above to determine the four-momentum of produced $\bar{p}$'s, a longitudinal (z) position within the interaction region is chosen for each produced $\bar{p}$. These are selected randomly from the geometrically weighted distribution weight$(z)=(R^2-z^2)$, where R is the radius of the interaction region (which is assumed to be spherical). Then each $\bar{p}$ is boosted in the longitudinal direction, using a boost velocity determined by the z position:

$$\beta_l(z)=\beta_l^{\max}\times\frac{z}{R}. \tag{5}$$

The results of this calculation are shown in Fig. 10, for values of $\beta_l^{\max}$ ranging from 0.4 to 1.0. For increasing values of $\beta_l^{\max}$, the distribution broadens, as would be expected. However, in order to achieve a rapidity width which is consistent with the measured E878 data, a value of $\beta_l^{\max}=1.0$ must be used, which is not a physically possible choice. Because only longitudinal expansion has been included, no particles have been boosted out of the E878 p_t acceptance. Thus, the area under each of the curves is the same as that of the original (no expansion) histogram; longitudinal expansion can force the model to match the shape of the E878 distribution, but it continues to overpredict the magnitude of $\bar{p}$ yields.

The expansion model can be made more realistic by including nonlongitudinal flow as well. The approach will be to consider an interaction region where all participating nucleons have completely stopped, consistent with the assumptions of the phase space/first collisions model. In this scenario of complete stopping, the longitudinal direction is no longer unique in the c.m. frame so that the interaction region expands radially in that frame. The recipe for implementing radial expansion is similar to that for longitudinal (detailed above), with the exception that a $\bar{p}$ production point is randomly chosen from within the entire sphere (weighted geometrically); the boost velocity will now be in the radial direction, with a magnitude determined by the radial position (r) of the production point, following

$$\beta_{\rm rad}(r)=\beta_{\rm rad}^{\max}\times\frac{r}{R}. \tag{6}$$

The results of this calculation are compared to E878 measurements in Fig. 11. As $\beta_{\rm rad}^{\max}$ increases, the zero degree distribution is both broadened and reduced in magnitude, since some of the antiprotons are being boosted out of the E878 p_t acceptance. Again, in order to force the shape to most closely match that observed by E878, an unphysical choice of $\beta_{\rm rad}^{\max}=1$ must be made. However, it is worth noting that in [38], a maximum transverse boost velocity of 0.58 achieved a good match to Si+Al central data for various particle species; a similar value of $\beta_{\rm rad}^{\max}=0.6$ applied to the phase space/first collisions distribution matches the E878 data points reasonably well (except for the highest rapidity points, where the phase space calculation breaks down even for the simplest systems). Interestingly, a similar maximum

transverse boost velocity of 0.60 has also recently been observed for various particle species produced in Pb+Pb collisions at the CERN SPS [41]. It is probably not wise to read too much into the agreement of the E878 boost velocity with these others, since the model used here differs in detail from that of [38,41] and a systematic study across several particle species would be necessary to judge how $\beta_{\rm rad}^{\rm max}$ in central Au+Au might compare to that of other systems. Nevertheless, this result is interesting in the sense that it implies that a reasonable estimate of hydrodynamic expansion may account for the suppression of $\bar{p}$ production at $p_t=0$ seen by E878. If this were true, it would suggest that, even for central Au+Au collisions, first collision scaling may still apply. However, given the limited p_t acceptance of E878, this question is still far from settled.

RQMD [42] attempts to describe the physics of relativistic heavy ion collisions microscopically via a semiclassical transport approach: nucleons in the target and projectile are propagated through the interaction region in small time slices, undergoing both elastic and inelastic binary interactions in the process. Any produced secondary particles are also propagated through the interaction region and allowed to undergo interactions. Given the large number of initial nucleons and produced secondaries, these calculations are very complex and require a great deal of computing time to perform; thus, statistics are at a premium. In order to maximize statistics for antiprotons, production of antibaryons is increased by boosting the appropriate branching fractions by an order of magnitude; this factor must then be divided back out in order to arrive at properly normalized antiproton cross sections.

RQMD allows for the formation of high-lying resonances, using a continuum of energy states beyond those measured experimentally [35]; this mechanism results in a substantial increase in $\bar{p}$ production. In modeling annihilation, RQMD uses measured free-space annihilation cross sections, which results in the absorption of a large fraction of the produced antiprotons (e.g., $\sim$90% of $\bar{p}$'s are reabsorbed for minimum bias Au+Au collisions [28]).

The comparisons which follow are based on RQMD version 1.07, which has been run in ''cascade mode'' (which neglects the effects of potentials between particles). As will be discussed below, a newer version of RQMD (RQMD 2.2) has been produced since the first appearance of the E878 $\bar{p}$ data [18,43], so that to some extent these comparisons are dated. However, comparisons to the earlier version graphically illustrate the effect of $\bar{p}$ annihilation, and as such are very useful in trying to understand the dynamics of $\bar{p}$'s within the heavy ion environment.

In order to simulate the E878 acceptance, a $p_t<200$ MeV cut has been applied to the model. This cut somewhat overestimates the E878 transverse momentum acceptance, but was necessary in order to achieve reasonable antiproton statistics. However, in calculating predicted cross sections, the magnitude of the transverse momentum bite is part of the normalization; thus, it is not crucial that the range included actually match the E878 acceptance, as long as $\bar{p}$ production is relatively flat over that range. When comparing to E878 measurements for the various defined centrality bins, the

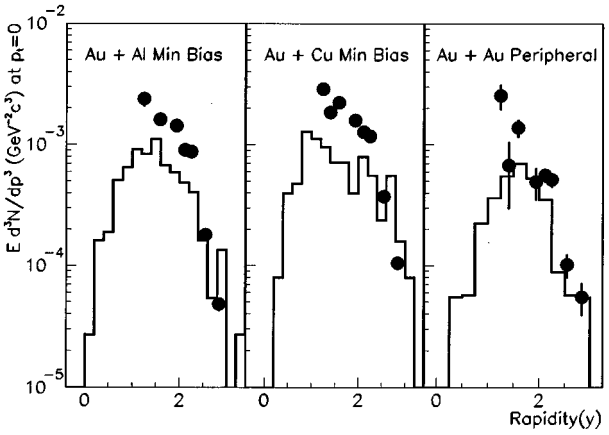

FIG. 12. $\bar{p}$ rapidity distributions for minimum bias Au+Al and Au+Cu events, and for the 30% most peripheral Au+Au events. RQMD predictions are shown as solid histograms; E878 measured data are shown as solid symbols.

RQMD events have been characterized in bins of impact parameter and $\bar{p}$ rapidity distributions are determined for each of these (1 fm) bins. Then, these histograms are added, using the impact parameter distributions of the centrality bins (as determined by GEANT simulation, with RQMD as an event generator) as weight factors. Model predictions using this method do not significantly differ from those calculated using a simple impact parameter cut corresponding to the appropriate fraction of the total interaction cross section.

Shown in Fig. 12 are comparisons for Au+Al minimum bias, Au+Cu minimum bias and Au+Au peripheral events. Note that for the two minimum bias spectra, geometric weighting of impact parameters determines that the majority of these events will be peripheral. For these systems, the collision region is expected to be (relatively) small, the baryon density to be (relatively) low, and collective effects to not be as important as they will be for central events. In that sense, these comparisons primarily assess the ability of the model to describe $\bar{p}$ production through simple *N*-*N* channels, with minimal absorption. RQMD does a good job of matching the E878 measurements for the peripheral Au+Au events, which is the simplest system of the three considered. However, even in the fairly simple systems of minimum bias Au+Al and Au+Cu, $\bar{p}$ annihilation significantly affects the RQMD spectrum, as evidenced by a shift toward target rapidity. This shift appears to be more pronounced than any shift seen in the E878 data; however, the lack of E878 data at points below midrapidity precludes any conclusive statement.

A comparison for $\sim$10% central Au+Al, Au+Cu, and Au+Au collisions are shown in Fig. 13. Again, in the asymmetric systems, RQMD displays a shift toward target rapidity; the E878 points are rather inconclusive on the matter of a rapidity shift. However, for both central Au+Al and Au+Cu events, RQMD significantly underpredicts the $\bar{p}$ yield in the midrapidity region. For central Au+Au collisions, RQMD underpredicts by a factor of $\sim$3 near midrapidity. The importance of annihilation in the RQMD model is apparent from the dip at midrapidity; no such suppression is present in the E878 data.

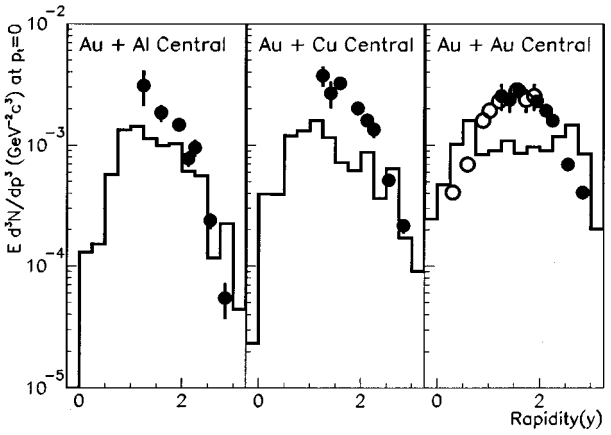

FIG. 13. $\overline{p}$ rapidity distributions for 10% central Au+Al, Cu, and Au events. RQMD predictions are shown as solid histograms. E878 measured data are shown as solid symbols; for Au+Au, data reflected about y_{nn} are shown as open symbols.

Shown in Fig. 14 are the RQMD predictions and the E878 measured data for the four defined centrality bins in Au+Au collisions. The model does a good job for the peripheral bin (as seen earlier); however, for the midperipheral bin, RQMD begins to show the effect of significant annihilation by underpredicting near midrapidity. This same trend continues for the midcentral and central bins where RQMD systematically underpredicts.

The underlying theme of these comparisons is the critical importance of the annihilation process on both the shape and magnitude of the observed $\overline{p}$ spectrum. In order for antiprotons to be used as a reliable probe of the collision environment, this process needs to be well understood. Given the sheer magnitude of the annihilation process, achieving this understanding is difficult, but perhaps not impossible.

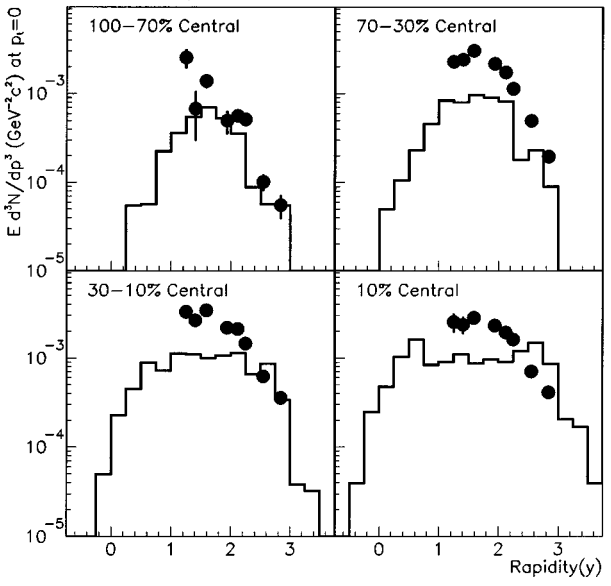

FIG. 14. $\overline{p}$ invariant multiplicity as a function of rapidity for each of the defined centrality bins in Au+Au events. E878 measured data are shown as solid symbols, and the RQMD 1.07 prediction is shown as a solid line.

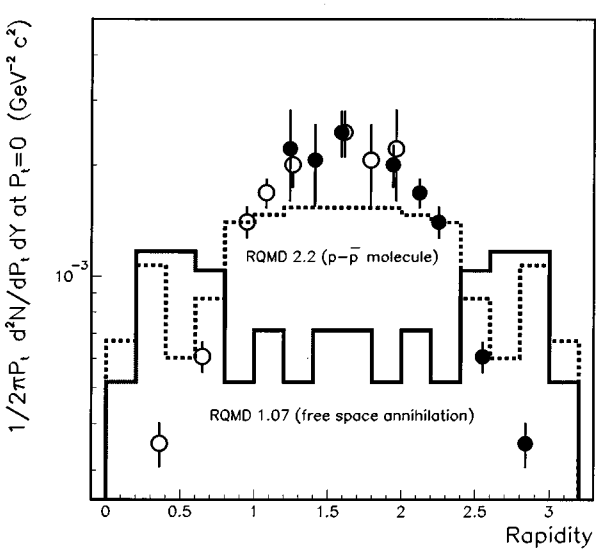

FIG. 15. E878 measured $\overline{p}$ yields for 10% central Au+Au events, compared to predictions of RQMD 1.07 (shown as solid lines), where $\overline{p}$ annihilation is modeled using the full free space cross section, and RQMD 2.2 (shown as dashed lines), where $\overline{p}$ annihilation is reduced due to the formation of a $\overline{p}$-p molecule. E878 measured data are shown as solid symbols; open symbols are data reflected about y_{nn}.

The possibility that antiproton annihilation may be reduced in the high densities of heavy ion collisions was first proposed in the ARC model [9], through screening of the annihilation process via a third body interaction. As contrasted to the RQMD predictions shown above, the most recent version of RQMD (RQMD 2.2) uses a new approach to antiproton annihilation [12]. As antiprotons are propagated through the interaction region, a Breit-Wigner formalism is used to allow the formation of a proton-antiproton molecule with a lifetime of 1 fm/c. The existence of this state is based on a parametrization of the shape of the antiproton annihilation cross section spectrum, as a function of relative momentum of the pair. The formation of this quasibound state significantly reduces the possibility of antiproton annihilation, as shown in Fig. 15 for central Au+Au collisions. The agreement with the E878 data is much improved by this new description, suggesting that annihilation is indeed suppressed (as compared to free space cross sections) in hot and dense environments. A systematic comparison of RQMD 2.2 to E878 data, and that of other experiments, should be useful in refining this approach and in understanding the annihilation process in relativistic heavy ion collisions.

The shape of observed antiproton yields can also be affected by processes not included in the ''cascade'' versions of models, specifically by mean Coulomb and color potentials. Using the formalism of Shuryak [44] and an estimate of the number of comoving protons at midrapidity performed by Gonin [36], it is estimated that the inclusion of Coulomb effects in RQMD would increase the central Au+Au $\overline{p}$ yield at midrapidity by no more than 20%, while the highest rapidity point changes by less than 10%. This adjustment is at the level of the bin-to-bin statistical scatter in the model predictions for this system shown in Fig. 13. Thus, the inclusion of Coulomb effects would not significantly change the

shape of the model predictions shown in the previous section; they certainly would not be sufficient to fill in the dip at midrapidity predicted by RQMD. However, mean color potentials could possibly have a much more significant effect on the final antiproton distributions. Spieles *et al.* have investigated the impact of mean color fields, in the form of an antinucleon-nucleus optical potential, on the $\bar{p}$ phase space distributions predicted by RQMD [13], with the result that the shapes of the predicted zero degree spectra are much closer to the E878 measurements for central Au+Cu and Au+Au events. Thus, while the success of RQMD 2.2 in matching the E878 spectra is highly suggestive that antiproton annihilation is indeed suppressed in the heavy ion environment, this question cannot be fully settled until antiproton yields have been measured over all phase space.

V. SUMMARY AND CONCLUSIONS

In summary, E878 has performed a high statistics study of $\bar{p}$ yields at $p_t=0$ in Au+A collisions, covering a broad kinematic range. Using this data, $\bar{p}$ yields measured for Au+A have been compared to those which might be expected from the superposition of independent nucleon-nucleon collisions in the context of a simple phase space/first collisions model. For increasing size of the interaction region, zero degree $\bar{p}$ rapidity distributions display a substantial increase in rms width, which has been attributed to a combination of increased energy available for $\bar{p}$ production through the formation of resonances, hydrodynamic expansion of the interaction region, and increasing contributions from $\bar{\Lambda}$ decays at high rapidity. For increasing size of the interaction region, total $\bar{p}$ yield at $p_t=0$ is substantially suppressed from a linear dependence on the number of first collisions. This trend is in contrast to the results published by the E814 Collaboration, which found that total $\bar{p}$ yields displayed a linear dependence on the number of interacting projectile nucleons for the lighter Si+A systems [19]. However, it has been shown that hydrodynamic expansion can lead to a decrease in $\bar{p}$ yields at $p_t=0$; further, using a reasonable estimate of expansion velocity in the context of a phase space/first collisions model, a reasonably good match to E878 central Au+Au data has been accomplished. This result suggests that hydrodynamic expansion may account for nearly all of the observed suppression of $\bar{p}$'s relative to a linear dependence on the number of first collisions. Thus, in the context of first collision scaling, the E878 antiproton yields do not appear to be consistent with a large enhancement in production, which has been predicted to be a signature of QGP formation [6,7].

RQMD (version 1.07) matches E878 well for the simplest system; however, for central events, RQMD shows both a rapidity shift for asymmetric systems and a dip at midrapidity for Au+Au, neither of which are apparent in the E878 measurements. In the most recent version of RQMD (RQMD 2.2) [12], the addition of an antiproton-proton quasibound state reduces annihilation and greatly improves agreement with E878 data from central Au+Au events. These results suggest that there may be a suppression of annihilation as compared to that expected from the free-space annihilation cross section.

ACKNOWLEDGMENTS

The authors would like to thank H. Sorge and C. Spieles for help with RQMD events and for illuminating discussions. We also thank the AGS personnel for providing the Au beams. This work has been supported in part by Grants No. DE-FG02-91ER-40609, No. DE-FG03-88ER-40424, and No. DE-FG03-90ER-40571 with the U.S. Department of Energy.

[1] J. Carroll *et al.*, Phys. Rev. Lett. **62**, 1829 (1989).
[2] A. Jahns, H. Sorge, H. Stöcker, and W. Greiner, Z. Phys. A **341**, 243 (1992).
[3] V. Metag, Prog. Part. Nucl. Phys. **30**, 75 (1993).
[4] C. Spieles, A. Jahns, H. Sorge, H. Stöcker, and W. Greiner, Mod. Phys. Lett. A **8**, 2547 (1993).
[5] V. Koch, G. E. Brown, and C. M. Ko, Phys. Lett. B **265**, 29 (1991).
[6] U. Heinz, P. R. Subramanian, H. Stöcker, and W. Greiner, J. Phys. G **12**, 1237 (1986).
[7] J. Ellis, U. Heinz, and H. Kowalski, Phys. Lett. B **233**, 223 (1989).
[8] C. B. Dover, T. Gutsche, M. Maruyama, and A. Faessler, Prog. Part. Nucl. Phys. **29**, 87 (1992).
[9] S. Kahana, Y. Pang, T. Schlagel, and C. B. Dover, Phys. Rev. C **47**, 1356 (1993).
[10] J. Costales, Ph.D. thesis, Massachusetts Institute of Technology, 1990.
[11] B. S. Kumar, S. V. Greene, and J. T. Mitchell, Phys. Rev. C **50**, 2152 (1994).
[12] H. Sorge, J. L. Nagle, and S. Kumar, Yale Report No. 40609-1233.
[13] C. Spieles, M. Bleicher, A. Jahns, R. Mattiello, H. Sorge, H. Stöcker, and W. Greiner, Phys. Rev. C **53**, 2011 (1996).
[14] D. Beavis *et al.*, Phys. Rev. Lett. **75**, 3633 (1995).
[15] D. Beavis *et al.*, Phys. Rev. Lett. **75**, 3078 (1995).
[16] M. Aoki *et al.*, Phys. Rev. Lett. **69**, 2345 (1992).
[17] P. Stankus, Ph.D. thesis, Columbia University, 1993.
[18] M. J. Bennett, Ph.D. thesis, Yale University, 1995.
[19] J. Barrette *et al.*, Phys. Rev. Lett. **70**, 1763 (1993).
[20] S. V. Greene, Ph.D. thesis, Yale University, 1992.
[21] T. Abbott *et al.*, Phys. Lett. B **271**, 447 (1991).
[22] T. Abbott *et al.*, Phys. Rev. C **47**, 1351 (1993).
[23] P. Rothschild, Ph.D. thesis, Massachusetts Institute of Technology, 1994.
[24] G. E. Diebold *et al.*, Phys. Rev. C **48**, 2984 (1993).
[25] The 859 Collaboration, Y. Wu *et al.*, in Heavy Ion Physics at the AGS (HIPAGS 96), edited by C. A. Pruneau, G. Welke, R. Bellwied, S. J. Bennett, J. R. Hall, and W. K. Wilson, Wayne State University, Detroit, Michigan, 1996, WSU-NP-96-16 (unpublished), p. 37.

[26] J. Lajoie, Ph.D. thesis, Yale University, 1996; F. Rotondo, for the E864 Collaboration, Nucl. Phys. **A610**, 297c (1996).
[27] H. J. Crawford and T. J. Hallman, spokesmen, E896 Proposal to BNL-AGS (unpublished).
[28] A. Jahns, C. Spieles, R. Mattiello, H. Sorge, N. S. Amelin, H. Stöcker, and W. Greiner, Nucl. Phys. **A566**, 483 (1994).
[29] P. Pile (private communication).
[30] P. Braun-Munzinger *et al.*, E877 Internal Note 1 (unpublished).
[31] D. Beavis *et al.*, Nucl. Instrum. Methods Phys. Res. A **357**, 283 (1995).
[32] D. Carey, Fermilab National Accelerator Laboratory Report No. NAL-64, 1978 (unpublished).
[33] K. Brown *et al.*, TRANSPORT: A Computer Program for Designing Charged Beam Transport Systems, Report No. SLAC-91 (unpublished).
[34] T. F. Hoang, B. Cork, and H. J. Crawford, Z. Phys. C **29**, 611 (1985).
[35] A. Jahns, H. Stöcker, and W. Greiner, Phys. Rev. Lett. **68**, 2895 (1992).
[36] M. Gonin, for the E802 Collaboration, Nucl. Phys. **A566**, 601 (1994).
[37] J. Cugnon and J. Vandermeulen, Ann. Phys. (Paris) **14**, 49 (1989).
[38] P. Braun-Munzinger, J. Stachel, J. P. Wessels, and N. Xu, Phys. Lett. B **344**, 43 (1995).
[39] M. Hofmann *et al.*, Nucl. Phys. **A566**, 15 (1994).
[40] R. Brun *et al.*, GEANT Users's Guide, Program Library W5013, CERN, 1993 (unpublished).
[41] I. G. Bearden *et al.*, Phys. Rev. Lett. **78**, 2080 (1997).
[42] H. Sorge, H. Stöcker, and W. Greiner, Nucl. Phys. **A498**, 266 (1989).
[43] M. J. Bennett, for the E878 Collaboration, Nucl. Phys. **A590**, 491c (1995).
[44] E. Shuryak, Nucl. Phys. **A533**, 761 (1991).